

X-shaped Radio Galaxies: Optical Properties, Large-scale Environment and Relationship to Radio Structure

RAVI JOSHI,¹ GOPAL-KRISHNA,^{2,3} XIAOLONG YANG,^{1,4} JINGJING SHI,¹ SI-YUE YU,^{1,5} PAUL J. WHITA,⁶ LUIS C. HO,^{1,5}
XUE-BING WU,^{1,5} TAO AN,⁴ RAN WANG,^{1,5} SMITHA SUBRAMANIAN,⁷ AND HASSEN YESUF¹

¹*Kaoli Institute for Astronomy and Astrophysics, Peking University, Beijing 100871, China*

²*Aryabhata Research Institute of Observational Sciences ARIES, Manora Peak, Nainital, Uttarakhand 263002, India*

³*UM-DAE Centre for Excellence in Basic Sciences, University of Mumbai, Mumbai 400098, India*

⁴*Shanghai Astronomical Observatory, Key Laboratory of Radio Astronomy, Chinese Academy of Sciences, 200030 Shanghai, P.R. China*

⁵*Department of Astronomy, School of Physics, Peking University, Beijing 100871, China*

⁶*Department of Physics, The College of New Jersey, PO Box 7718, Ewing, NJ 08628-0718, USA*

⁷*Indian Institute of Astrophysics, Sarjapur Main Road, Koramangala II Block, Bangalore, Karnataka 560034, India*

ABSTRACT

In order to find clues to the origin of the "winged" or X-shaped radio galaxies (XRGs) we investigate here the parent galaxies of a large sample of 106 XRGs for optical-radio axes alignment, interstellar medium, black hole mass, and large-scale environment. For 41 of the XRGs it was possible to determine the optical major axis and the primary radio axis and the strong tendency for the two axes to be fairly close is confirmed. However, several counter-examples were also found and these could challenge the widely discussed backflow diversion model for the origin of the radio wings. Comparison with a well-defined large sample of normal FR II radio galaxies has revealed that: (i) XRGs possess slightly less massive central black holes than the normal radio galaxies (average masses being $\log M_{\text{BH}} \sim 8.81 M_{\odot}$ and $9.07 M_{\odot}$, respectively); (ii) a much higher fraction of XRGs ($\sim 80\%$) exhibits red mid-IR colors ($W2 - W3 > 1.5$), indicating a population of young stars and/or an enhanced dust mass, probably due to relatively recent galaxy merger(s). A comparison of the large-scale environment (i.e., within ~ 1 Mpc) shows that both XRGs and FR II radio galaxies inhabit similarly poor galaxy clustering environments (medium richness being 8.94 and 11.87, respectively). Overall, the origin of XRGs seems difficult to reconcile with a single dominant physical mechanism and competing mechanisms seem prevalent.

Keywords: galaxies: evolution, galaxies: kinematics and dynamics, galaxies: active, galaxies: star formation, galaxies: radio galaxies, galaxies: supermassive black holes

1. INTRODUCTION

X-shaped radio galaxies (XRGs) constitute a small but significant fraction (up to $\sim 3 - 10\%$) of radio galaxies (Leahy & Williams 1984; Leahy & Parma 1992; Yang et al. 2019). They exhibit two misaligned pairs of radio lobes with the fainter pair (called 'radio wings') being edge-darkened and the brighter pair (called 'primary' or 'active' lobes) being usually edge-brightened, like the classical (FR II) double radio sources (Leahy & Williams 1984; Capetti et al. 2017). While it is generally accepted that the primary lobes are created by a pair of powerful radio jets emanating from the

central active galactic nucleus (AGN), the origin of the secondary pair (wings) continues to be debated.

The proposed theoretical explanations for the origin of 'wings' fall in two broad categories: (i) intrinsic, i.e., pivoted on the central engine, and (ii) extrinsic, wherein the external environment plays the paramount role (see, Gopal-Krishna et al. 2010, for a review). According to one popular scenario in the second category, the wings form due to diversion of the backward flowing synchrotron plasma within the two radio lobes, as it impinges on an asymmetric circum-galactic gaseous halo of the parent (early-type) galaxy and is propelled by the buoyancy forces along the direction of the steepest pressure gradient in the surrounding medium (Leahy & Williams 1984; Worrall et al. 1995; Kraft et al. 2005; Capetti et al.

2002; Hodges-Kluck et al. 2010b; Rossi et al. 2017). For this “backflow diversion” model to work, the radio lobes are required to be of the FR II type, which alone are capable of sustaining a strong backflow and the absence of hot spots in the wings is then naturally explained. Strong support to this picture has come from the optical studies of a small number of XRGs, which have clearly shown that the direction defined by the pair of radio wings exhibits a clear preference to be closer to the optical minor axis of the host elliptical galaxy and the converse holds for the primary lobes (Capetti et al. 2002; Saripalli & Subrahmanyan 2009; Gillone et al. 2016). Additional support has come from the X-ray studies by Hodges-Kluck et al. (2010a) showing that the wings tend to align with the minor axis of the hot gaseous halo of the parent galaxy. However, existence of some XRGs with primary lobes of FRI type might challenge this backflow diversion scenario (but see, Saripalli & Subrahmanyan 2009).

In the intrinsic class of models, the X-shaped radio morphology is explained in terms of a rapid change in the jet ejection direction, i.e., a reorientation/flip of the spin axis of the supermassive black hole (SMBH), either due to merger of a small galaxy with the massive elliptical host of the radio source (Zier & Biermann 2001; Merritt & Ekers 2002; Rottmann 2001; Zier & Biermann 2002), or due to accretion disk instabilities (Dennett-Thorpe et al. 2002). In the former, so called ‘spin-flip’ scenario, the wings are viewed as relics of their pre-merger active phase. Indeed, this model accords well with the widely discussed scenario for powerful double radio galaxies, wherein a galaxy merger of a gas-rich galaxy with the massive elliptical triggers the jet activity in the massive elliptical (Begelman et al. 1984; Wilson & Colbert 1995). Whilst this scenario appears to have found some observational support from the detection of SMBH binary within the nuclei of a few AGN (Rodriguez et al. 2006; Kharb et al. 2017), and also from the discovery of double-peaked broad emission lines in a few AGN (Zhang et al. 2007; Rubinur et al. 2019), it offers no clear explanation for the propensity of the primary radio lobes in XRGs to be aligned close to the optical major axis of the parent elliptical galaxy.

Recently, using GMRT observations of 28 XRGs at 610 MHz and 240 MHz, Lal et al. (2019) have found no systematic difference between the radio spectral indices of the primary radio lobes and the wings (see also, Lal & Rao 2005, 2007). This appears to be at odds both the ‘backflow diversion’ and the ‘spin-flip’ scenarios. To address this, Lal & Rao (2005, 2007) have put forward the ‘twin-AGN’ hypothesis wherein the two pairs of

lobes are powered by two independent jet pairs emanating from an unresolved pair of central engines. However, this picture does not explain the preference of the radio wings’ pair to be aligned close to the optical minor axis of the host elliptical galaxy.

In this context, it is interesting to recall the suggestion that the jets can be intercepted by rotating segments of stellar/gaseous shells like those which have been detected around a number of nearby early-type galaxies (Carter et al. 1982; Schiminovich et al. 1994; Oosterloo & Morganti 2005; Sikkema et al. 2007; Struve & Conway 2010; Mancillas et al. 2019). Earlier, such a scenario of jet-shell interaction has been invoked to explain certain intriguing radio features witnessed in the nearest radio galaxy Centaurus A, particularly its peculiar “North Middle Lobe” (Gopal-Krishna et al. 2010, hereafter GKW10) and the “North Inner Lobe” (Gopal-Krishna & Saripalli 1984; Gopal-Krishna & Chitre 1983). Plausibly, such interactions take place also in XRGs, which would provide a straight-forward explanation for the strong tendency for their primary lobes to align with the optical major axis of the host elliptical, as discussed in Gopal-Krishna et al. (2003, 2012, , hereafter GBW03, GBGW12). Such putative shells have since also been detected in a few (more distant) elliptical galaxies hosting an XRG, such as 3C 403 and 4C+00.58 (Hodges-Kluck et al. 2010b; Ramos Almeida et al. 2011; Tadhunter 2016).

The Z-symmetry of the radio wings in XRGs, highlighted in Gopal-Krishna et al. (2003) has motivated a hybrid model which reconciles the spin-flip scenario with the striking Z-symmetry of the wings and, moreover, can easily explain why some wings are longer than the associated primary lobes (see discussion in Section 5). In this model, the observed Z-symmetric radio wings form via a bending of the twin-jets in opposite directions upon their interacting with the ISM which has been set in ordered rotation due to the in-spiralling of a gas-rich galaxy captured by the jet-emitting massive elliptical. Later, as the central black holes of the two merging galaxies coalesce, the SMBH spin axis (and hence the axis of the emergent jet pair) would get aligned towards the initial orbital momentum vector of the captured galaxy. Thus, since after the spin-flip, the direction of the twin-jets would be close to the ISM rotation axis, their outward propagation to form the primary lobe pair, would no longer receive a side-way push from the the rotating ISM, which would facilitate their linear propagation (Gopal-Krishna et al. 2003). As argued in GBW03 and GBGW12 (see, also, Hodges-Kluck & Bregman 2014), such a model can also explain in a natural way the curious result that radio

luminosities of XRGs tend to cluster near the Fanaroff-Riley transition, i.e. $P_{178} \text{ MHz } 10^{25} \text{ WHz}^{-1} \text{ sr}^{-1}$.

It needs to be appreciated that the afore-mentioned observational clues are still based on rather small samples, namely 11 XRGs found in the 3CR catalog (Leahy & Parma 1992) and 100 XRG candidates identified in a systematic search based on the FIRST survey (Cheung 2007). Recently, we have expanded the sample by preparing a new catalog of 290 XRG candidates, primarily based on of 1.4 GHz FIRST and the TIFR GMRT sky survey (TGSS) made at 150 MHz (Yang et al. 2019). This latest catalog of XRG candidates is an extension to smaller angular sizes of the XRG search undertaken by Cheung (2007), which led to a catalog of 100 XRG candidates, nearly $\sim 75\%$ of which were confirmed as bona-fide XRGs, in follow-up VLA observations (Roberts et al. 2018). In our catalog of 290 XRG candidates, 106 were classified as ‘strong’ XRG candidates and only this subset will be used in the present study to explore the salient scenarios proposed to understand the XRG phenomenon. In particular, we shall endeavor to examine the geometrical/morphological relationship between the radio lobes and the optical host galaxy, as well as the possible relevance of galaxy merger and large-scale environment to the occurrence of XRGs.

This paper is organized as follows. Section 2 describes our sample of XRGs, as well as a control sample comprised of normal FR II radio galaxies. In Section 3, we examine the geometrical relationship between radio and optical morphologies of XRGs. Section 4 presents a comparison of the XRGs and FR II radio galaxies in terms of optical spectral line properties and galaxy estimates. The discussion and conclusions of this study are summarized in Section 5. Throughout, we have assumed the flat Universe with $H_0 = 70 \text{ km s}^{-1} \text{ Mpc}^{-1}$, $\Omega_m = 0.3$ and $\Omega_\Lambda = 0.7$.

2. THE XRG SAMPLE

Our starting point is the sample of 106 strong XRG candidates, extracted from the compilation of 290 winged radio galaxies published recently by some of us (Yang et al. 2019). In brief, we extended the catalog of 100 XRGs with radio major axis, $\theta_{major} \geq 15 \text{ arcsec}$ (Cheung 2007) to smaller angular sizes, i.e., considering sources with θ_{major} down to 10 arcsec. The resulting catalog of 290 XRG candidates, mainly based on the 1.4 GHz FIRST and 150 MHz TIFR GMRT sky survey (TGSS), includes 106 ‘strong’ XRG candidates in which at least one of the two wings is well defined (Section 1).

Given that the active (primary) radio lobes of XRGs are overwhelmingly of the FR II type and they predomi-

nantly occupy the domain of FR II sources in the Owen-Ledlow Plane (see, Section 1; Yang et al. 2019), we are motivated to carry out a comparison of the properties of the XRGs with those of FR II radio galaxies. For this, we have used a sample of 401 FR II radio galaxies from Kozieł-Wierzbowska & Stasińska (2011) for which optical spectra are available in the SDSS, except for one object. Out of these 400 FR II radio galaxies with spectra, we have excluded ten, as they exhibit ‘double-double’ radio morphology (Schoenmakers et al. 2000) and another two sources which have been re-classified as XRGs by Kuźmicz et al. (2017). These exclusions limit the control sample to 388 FR II radio galaxies.

Compared to the Cheung (2007) catalog, our source catalog of 290 XRG candidates admits only sources of smaller radio (angular) extent and spans a larger redshift range ($0.06 \leq z \leq 0.7$, with median $z \sim 0.37$). Hence, for a more general comparison with the control sample of FR II radio galaxies which spans a wide range in radio power and size, we have expanded our XRG sample by including the 11 XRGs reported in Leahy & Parma (1992) and the 100 XRG candidates cataloged by Cheung (2007). We have used information available in the literature for them.

3. OPTICAL VERSUS RADIO STRUCTURAL ALIGNMENT

To explore the geometric relationship between the radio structure and the parent elliptical galaxy, the first step was to determine the optical major axis of the elliptical. For this we mainly used the SDSS *i*-band images. Among the 106 strong XRG candidates (taken here as bona-fide XRGs), 7 sources have no optical object in the SDSS at the location of the host galaxy expected from the symmetry consideration of the radio lobes. For another 11 XRGs not covered in SDSS, we have used the *r*-band images from the DECam Legacy Survey [DECaLS] (Dey et al. 2018). Three XRGs are covered neither in SDSS nor in DeCaLS. This left us with 96 XRGs with detected optical hosts.

For each of these XRGs, elliptical isophotes were fitted to the optical image using the IRAF¹ task ‘Ellipse’ (Jedrzejewski 1987). In brief, we fitted the isophotes with sampling radius increasing exponentially in step of 1.1, and then characterized the galaxy ellipticity and position angle as well as their respective uncertainties as the mean value and standard deviation over the profiles

¹ IRAF is distributed by the National Optical Astronomy Observatory, which is operated by the Association of Universities for Research in Astronomy, Inc., under cooperative agreement with the National Science Foundation.

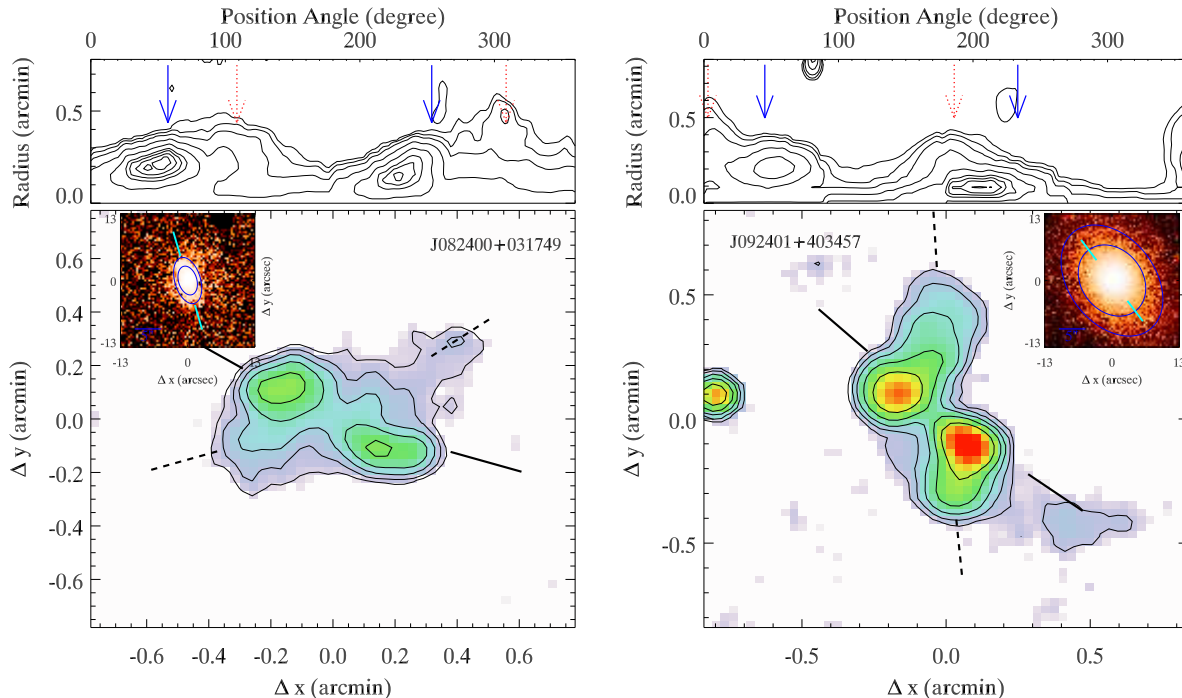


Figure 1. *Lower Left Panel:* The FIRST image of the XRG J000450+124839 at 1.4 GHz and the corresponding contours starting at 3σ level. The axes of the radio wings and the primary lobes are shown by dotted and solid lines, respectively. The inset shows the (*i*-band) SDSS image together with its major axis and the fitted ellipses (blue curves). *Upper illustration:* Polar diagram of the FIRST radio map at 1.4 GHz. The contours start at 3 times the local rms noise level in the map (typically at ~ 0.5 mJy/beam). The two bright peaks (blue arrows) mark hot spots in the two primary lobes, whereas the pair of radio wings can be identified with the linear extended features (red arrows). These identifiers yield quantitative estimates of the PAs of the primary and secondary radio axes defined by the pairs of the primary lobes and the wings, respectively. *Right Panel:* The same for the XRG J092401+403457.

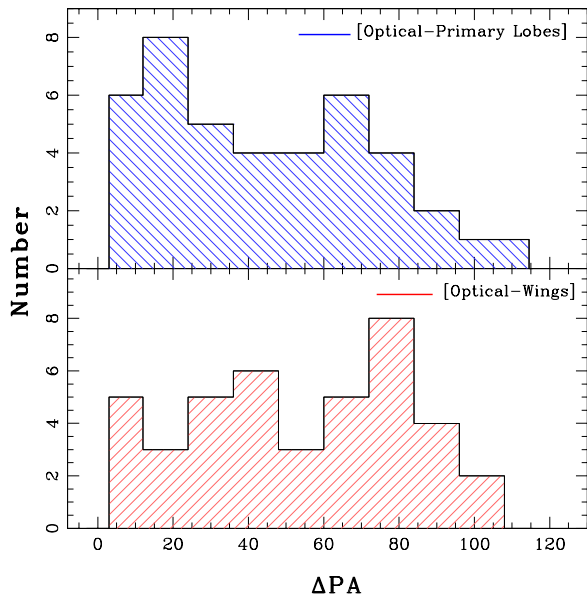


Figure 2. *Lower Panel:* Histogram of position angle offset of the optical main axis of the host elliptical from the axis defined by the pair of radio wings (secondary lobes). *Upper Panel:* the same for the pair of primary radio lobes.

in the outer part of the galaxy image, where the intensity is about 1σ above the sky level. A secure measurement of these quantities was often rendered difficult owing to the rather small angular size of the ellipticals, which is mainly due to their relatively large redshifts (median $z \sim 0.37$), as well as their rather shallow images in many cases. Therefore, we imposed a condition that the ellipticity must be above 0.1 (at $> 2\sigma$ level), which corresponds to the optical axial ratio > 1.1 , and, secondly, the estimated error on the measured position angle of the optical main axis should be $\lesssim 10$ degrees. Only 41 of the XRGs could satisfy these conditions imposed in the interest of reliability of the estimated parameters, as listed in columns 7 and 8 of Table 3 in Appendix A1.

Next, to estimate the position angle of the axes of the primary radio lobes and the wings, we constructed polar diagrams of the FIRST radio map at 1.4 GHz, taking the host galaxy as the origin (for details, see Gillone et al. (2016)). Using this diagram, we defined the position angle of the two radio wings as well as the primary lobes as the orientation of the wings (and the primary lobes) along the directions having the greatest distance from the center at which the brightness still exceeds the lo-

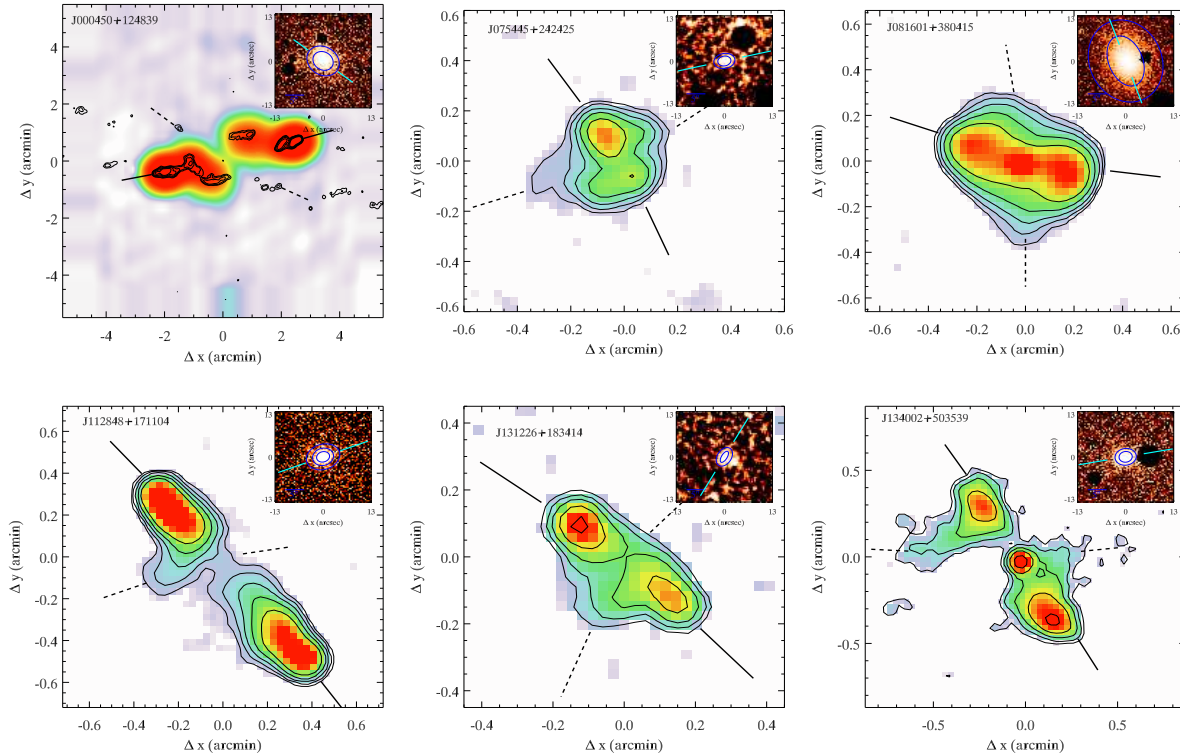


Figure 3. The 6 X-shaped radio galaxies where the radio wings are found to be aligned closer the optical major axis of the host elliptical. The inferred axes of the primary radio lobes and of the radio wings are marked with solid and dashed lines, respectively. The color images as well as the contours refer to the 1.4 GHz FIRST maps (except for J000450+124839 for which the color image represents the 1.4GHz NVSS map). The insets show the SDSS *i*-band image of the parent galaxies, whose optical major axes are marked with pairs of solid cyan lines.

cal 3σ noise level. The two examples shown in Fig. 1 (lower panels) display the measured radio position angle (PA) for the wings and the primary lobes, marked by dashed and solid lines, respectively. The upper panels contain the polar diagram showing the radio contours of the FIRST map in polar coordinates where the primary radio lobes produce the two main peaks and the diffuse extended wings produce the well defined linear features, indicating the position angle. The estimated PAs of the axes of the primary and secondary lobe pairs are listed in columns 3 and 5 of Table 3 in Appendix A1.

The afore-mentioned analysis has enabled examination of any geometrical linkage between the properties of the host galaxy and the associated X-shaped radio structure. Specifically, we have measured the position angle offsets between the major axis of the optical host (columns 3 and 4 of Table 1) from the axis defined by the two primary radio lobes (primary radio axis) and by the pair of the radio wings (secondary radio axis). Figure 2 shows the distributions of the two angular offsets. Note that we have taken average of the axes of the two paired radio lobes. It is evident that for the vast majority ($\sim 76\%$) of XRGs, the radio-optical posi-

tion angle offset for the secondary radio axis (defined by the two wings) is larger than 30° , with a median value of 57° . A Kolmogorov-Smirnov test (KS-test) rules out the null probability of being drawn from a uniform distribution at 0.05 significance level. This trend, first reported by Capetti et al. (2002) and most recently updated by Gillone et al. (2016), are both based on relatively small samples consisting of just 9 and 22 XRGs, respectively. The present analysis of a larger sample has further strengthens the claims that the radio wings in XRGs are preferentially aligned closer to the optical minor axis of the host elliptical galaxy. Interestingly, however, we do find 6 counter-examples, where the axis defined by the radio wings lies closer to the optical *major* axis of the host galaxy (see Fig. 3). The existence of even a handful of such counter-examples is interesting since it calls for caution in accepting the hydrodynamical explanation (i.e., the backflow diversion model) for the radio wings as the universal explanation for their formation (Section 1).

In Fig. 4, we have plotted the radio extents of the primary lobes and the associated wings for the 106 XRGs, as listed in columns 4 and 6 of Table 3. Note that the

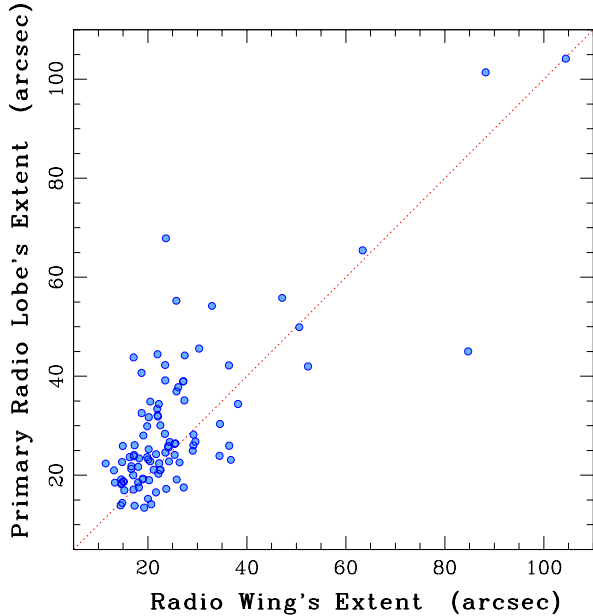


Figure 4. Distribution of the lengths of the primary and secondary lobes, for our sample of 106 XRGs.

usual definition of XRGs according to which the wing should extend at least 80% of the size of the associated primary lobe had been relaxed while constructing our XRG catalog (see section 2, Yang et al. 2019). This was intended to make an allowance for the fact that the detectability of the ‘tip’ of the radio wings can be hampered due to myriad factors, related to the sensitivity limitation and also the source evolution, its orientation and the wings’ directional offset from the primary lobe axis. Here we have plotted the larger of the two wings and of the two primary lobes in Fig. 4. It is seen that, taking an uncertainty of $\sim 10\%$ in measuring radio size, the fraction of XRGs having wings longer than the primary lobes can be as low as $\sim 20\%$ (the excess factor is > 1.5 in 3 cases). Note that in some of the XRGs, the wings could appear longer than the primary lobes merely due to foreshortening of the latter caused by orientation to our line of sight. Accounting for this could bring the apparent sizes more in tune with the basic backflow diversion scenario wherein a wing is expected to be intrinsically shorter than the primary lobe. On the other hand, since we are only concerned here with radio galaxies and not quasars, any foreshortening of the primary radio axis due to projection is not expected to be a major effect (in statistical terms). At this stage, it appears that an XRG having radio wings intrinsically longer than its active lobes is not a rare occurrence. Clearly, a satisfactory resolution of this issue would need deeper radio imaging at meter wavelengths.

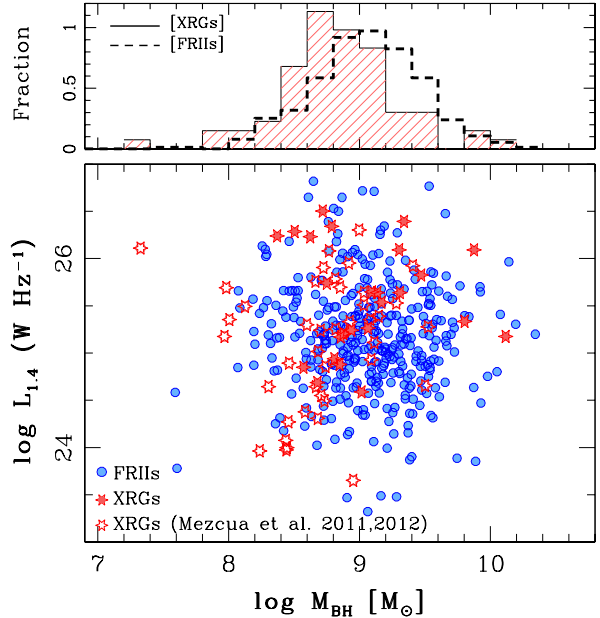


Figure 5. *Lower panel:* Relation between black hole mass (M_{BH}) and radio luminosity at 1.4 GHz for our 26 XRGs (filled stars), for the 41 XRGs from Mezcua et al. (2011, 2012) (open stars) and for the 388 FRII radio galaxies (circles). *Upper panel:* Distribution of M_{BH} found here for the 67 XRGs and 388 FRII radio galaxies.

4. OPTICAL SPECTRAL PROPERTIES

We now examine certain physical parameters of XRGs, derived from their optical spectra and then present a comparison with a large, well-defined, sample of normal FRII radio galaxies. Our analysis is based on the SDSS optical spectra which are available for 38 of our 106 XRGs. Six of these 38 had to be discarded as they are identified with quasars (including two showing double peaked narrow emission lines and no evidence for starlight). The reduced one-dimensional spectra for the remaining 32 XRGs and also for the control sample of 388 FRII radio galaxies were downloaded from the SDSS-BOSS Data Archive Server².

4.1. Masses of the Central Black Holes

To measure the required absorption and emission line parameters for the 32 XRGs and the control sample of 388 FRII galaxies (see Section 2), we first corrected each spectrum for reddening, taking the $E(B - V)$ values from Schlegel et al. (1998). This was followed up with spectral fitting using the penalized PiXel-Fitting method (pPXF, Cappellari & Emsellem 2004; Cappellari 2017). Briefly, pPXF works in the pixel space, and performs a nonlinear least-squares optimiza-

² <http://dr12.sdss3.org/bulkSpectra>

Table 1. Position angle offset of the axes defined by the pair of radio wings and by the two primary lobes, from the optical major axis of the host elliptical galaxy, for the 41 XRGs in which it was possible to measure all these parameters with reasonable accuracy.

Id	Name	Δ PA ^a	
		passive 1/2 (°)	active 1/2 (°)
1	J000450.27+124839.52	0/ 11	47/ 52
2	J002828.94−002624.60	67/ 86	76/ 77
3	J003023.86+112112.50	6/ 25	35/ 35
4	J012101.23+005100.38	59/ 55	30/ 33
5	J021635.79+024400.90	39/ 26	74/ 72
6	J031937.58−020248.70	44/ 45	5/ 7
11	J075445.52+242425.30	15/ −	58/ 69
15	J081404.55+060238.38	72/ 74	4/ 6
16	J081601.88+380415.48	5/ 14	56/ 68
17	J081841.57+150833.50	80/ 79	31/ 13
19	J082400.50+031749.30	84/ 66	44/ 59
21	J084509.65+574035.54	68/ 75	24/ 15
27	J092401.16+403457.29	24/ 22	17/ 24
28	J092802.68−060752.63	64/ 30	31/ 29
29	J093014.90+234359.20	70/ 44	72/ 71
32	J094953.64+445655.77	99/ 97	33/ 33
37	J103924.92+464811.53	52/ 50	53/ 62
38	J104632.43−011338.15	57/ 63	71/ 60
40	J112848.72+171104.57	1/ 12	69/ 75
42	J114522.19+152943.26	110/ 59	17/ 10
44	J115500.34+441702.22	92/ 70	1/ 1
45	J120251.32−033625.80	46/ 22	70/ 69
50	J131226.65+183414.98	13/ 8	92/ 82
51	J131331.40+075802.51	62/ 71	70/ 78
52	J132324.26+411515.01	114/ 49	16/ 13
53	J132404.20+433407.14	54/ 38	113/ 112
54	J132713.87+285318.19	45/ 45	24/ 14
56	J133051.04+024843.10	117/ 73	24/ 23
58	J134051.19+374911.74	45/ 43	107/ 106
59	J134002.96+503539.72	11/ 2	64/ 67
69	J150904.13+212415.10	62/ 58	50/ 50
71	J151704.61+212242.14	49/ 5	84/ 84
76	J155416.04+381132.57	99/ 76	39/ 44
77	J160809.55+294514.92	53/ 12	42/ 43
78	J162245.42+070714.69	42/ 44	7/ 7
79	J164857.36+260441.26	52/ 99	17/ 4
81	J202855.27+003512.67	29/ 26	47/ 44
86	J223628.89+042751.89	72/ 80	22/ 31
87	J232020.30−075319.36	92/ 100	40/ 43
99	J125721.87+122820.58	60/ 64	4/ 9
106	J203459.54+005221.41	91/ 86	29/ 17

^a Position angle difference between the optical major axis and passive lobes.

^b Position angle difference between the optical major axis and active lobes.

tion to provide the best-fit template and the velocity dispersion of the underlying stellar population. The emission lines in the de-reddened spectrum were masked and the underlying absorption spectrum was modeled as a combination of single stellar population templates with MILES (Vazdekis et al. 2010) which are available for

large ranges in the metallicity [M/H] (from ~ -2.32 to $+0.22$) and age (from 63 Myr to 17 Gyr).

Among the 32 XRGs, six have average SNR per pixel of < 3 , which is insufficient for a reliable measurement of a stellar velocity dispersion. Hence these could be obtained only for the remaining 26 XRGs, and are listed in column 4 of Table 2. We then proceeded with the estimation of mass of the central SMBH, using the well known tight relation: (Ferrarese et al. 2001; Gebhardt et al. 2000; Tremaine et al. 2002), given in Kormendy & Ho (2013, see their equation 3 and 7):

$$\frac{M_{\text{BH}}}{10^9 M_{\odot}} = (0.310_{-0.033}^{+0.037}) \left(\frac{\sigma_{*}}{200 \text{ km s}^{-1}} \right)^{4.38 \pm 0.29} \quad (1)$$

In the upper panel of Figure 5 we compare the SMBH mass distribution determined for the XRGs and for the control sample of 388 FR II radio galaxies. In this comparison, we have also included the 41 XRGs known earlier for which stellar velocity dispersions are available in Mezcua et al. (2011, 2012). The average M_{BH} for the FR II radio sources is found to be $M_{\text{BH}} = 9.07 M_{\odot}$, which is slightly higher than the average $M_{\text{BH}} = 8.81 M_{\odot}$ estimated for the 67 XRGs (see also, Kuźmicz et al. 2017). A two-sided Kolmogorov-Smirnov test shows that the population of XRGs and FR II radio sources are drawn from different distributions with KS -test null probability of $p_{\text{null}} = 0.005$. In the lower panel of Fig. 5 we look for any dependence of M_{BH} on the 1.4 GHz radio luminosity, for our set of 67 XRGs. The Spearman rank-correlation test does not show a significant correlation, with $r_s = 0.24$ and a null probability of $p_{\text{null}} = 0.04$.

4.2. Radio and optical emission-line luminosities

In order to measure the emission-line parameters we have modelled the emission line profiles as Gaussians superposed on the continuum subtracted spectrum. In brief, we first model the [S II] doublet lines which are taken to delineate the [N II] and H α narrow emission lines (Greene & Ho 2004). The satisfactory fit to the line shape, thus obtained, was used as a template for other narrow lines. Both the [S II] doublet lines were assumed to have equal widths (in velocity space) and be separated by their laboratory wavelengths. A single Gaussian profile provided a good fit in cases of all the XRGs, including the 16 XRGs where [S II] lies outside the spectral coverage of the SDSS. This analysis allowed us to place our XRGs in the BPT diagnostic diagram (Kewley et al. 2006) in which the intensity ratios of [O III] λ 5007 / H β are plotted against the ratios of [N II]/H α (Fig. 6). The value of these ratios, including upper limits, could be measured only for 17 of the 32 XRGs. We also display the same for a subset of 100

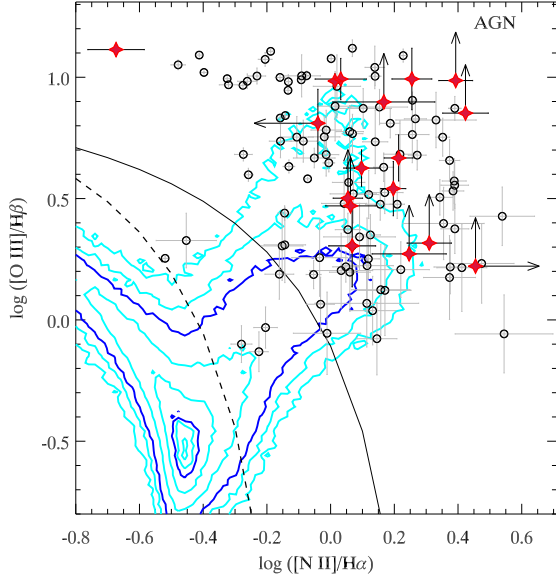


Figure 6. Diagnostic diagram: $[\text{O III}]/\text{H}\beta$ versus $[\text{N III}]/\text{H}\alpha$ for XRGs (red stars) and FRII comparison sample (open circles). The solid black line indicates the boundary between AGNs and star-forming galaxies, following Stasińska et al. (2006).

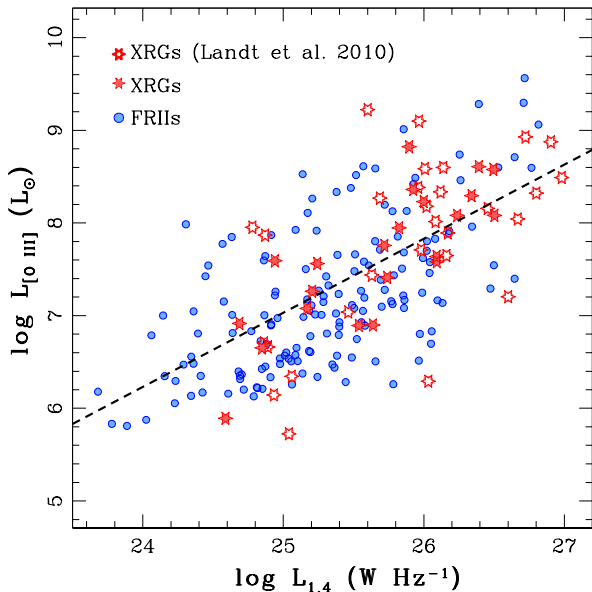


Figure 7. Radio luminosity at 1.4 GHz versus $[\text{O III}]\lambda 5007$ line luminosity (erg s^{-1}) for our XRGs (filled stars), XRGs from Landt et al. (2010) (stars) and the control sample of FRII radio galaxies (circles) by Kozieł-Wierzbowska & Stasińska (2011). The dashed line represents the best fit for the XRGs, as discussed in the text.

FRII radio galaxies (out of the control sample of total 388) for which the emission lines have been detected at $\geq 3\sigma$ level. Interestingly, all the 17 XRGs and nearly all of the 100 FRII galaxies are seen to inhabit the locus for AGNs wherein the emission lines are excited predominantly due to AGN activity. A similar trend has been noted by Gillone et al. (2016), based on a smaller sample of 11 XRGs.

For 3C radio sources, Rawlings et al. (1989) have reported a clear positive correlation between the luminosities of the 1.4 GHz emission ($L_{1.4}$) and the $[\text{O III}]\lambda 5007$ emission line ($L_{[\text{O III}]}$). This points to the existence of a coupling between the physical processes that power the narrow emission-line activity and the extended radio synchrotron emission. This correlation has been confirmed by Kozieł-Wierzbowska & Stasińska (2011) for their larger set of 401 FRII radio galaxies. In Fig. 7 we examine this for our XRG sample for which the values of $L_{[\text{O III}]}$ and 1.4 GHz luminosities are listed in columns 7 and 9 of Table 2. In the present analysis we have also included the 31 XRGs appearing in the catalog of 100 XRGs (Cheung 2007), for which $[\text{O III}]\lambda 5007$ line measurements are available in Landt et al. (2010). From Fig. 7, it is evident that a strong correlation between $[\text{O III}]\lambda 5007$ line luminosity and 1.4 GHz radio luminosity exists for XRGs, as well, and we can parameterise it as: $\log L_{[\text{O III}]} = [0.80 \pm 0.14] \log L_{1.4} - [12.97 \pm 3.58]$. The Spearman rank correlation test confirms the correlation with $r_s = 0.60$ with a null probability, $p_{null} = 2.1 \times 10^{-6}$ (i.e., significant at 4.3σ level).

Next, we classify the radio galaxies into low- and high-excitation classes (LERGs and HERGs) by following the criteria of Best & Heckman (2012) where a host galaxy with $[\text{O III}]\lambda 5007$ line of equivalent-width $> 5\text{\AA}$ is classified as HERG. The $[\text{O III}]\lambda 5007$ line equivalent-width and the corresponding spectral classification are listed for our XRG sample in column 8 and 10 of Table 2. Out of the 32 XRGs, 16 (i.e., 50%) are found to be HERGs, and the remaining 16 XRGs, including the 9 XRGs with only 3σ upper limit available for the $[\text{O III}]\lambda 5007$ line equivalent-width, fall in the category of LERGs.

4.3. Infrared properties of XRGs

We next investigate the mid-infrared properties of XRGs based on the Wide-field Infrared Survey Explorer (*WISE*) archival information. For this, we have searched for the *WISE* counterparts to the host galaxies of 225 XRGs, including our new 106 XRGs and the 119 XRGs assembled by Cheung (2007). *WISE* counterparts could also be found for the entire control sample of 388 FRII radio galaxies (note that only an offset of up to 3 arcsec between the SDSS and *WISE*

Table 2. Optical spectral parameters of the X-shaped radio galaxies.

Id	Name	z	σ_*	$\log M_{\text{BH}}$	$\log L_{[\text{OIII}]}$	$EW_{[\text{OIII}]}$	$\log L_{1.4\text{GHz}}$	spectral
(1)	(2)	(3)	[km s^{-1}]	[M_{\odot}]	[erg s^{-1}]	[\AA]	WHz^{-1}	type
			(5)	(6)	(7)	(8)	(9)	(10)
3	J003023.85+112112.4	0.449	—	—	42.41± 0.01	153.36 ± 2.25	24.69	HERG
4	J012101.23+005100.4	0.238	281 ± 46	9.1 ± 0.4	40.48± 0.07	2.84 ± 0.86	25.21	LERG
10	J072737.49+395655.5	0.312	470 ± 37	10.1 ± 0.3	<40.34	—	25.64	LERG
17	J081601.88+380415.3	0.173	286 ± 18	9.2 ± 0.2	40.48± 0.11	2.09 ± 0.84	25.54	LERG
20	J082400.50+031749.3	0.215	253 ± 31	8.9 ± 0.3	41.15± 0.02	8.12 ± 0.49	25.26	HERG
21	J084509.65+574035.7	0.237	241 ± 25	8.9 ± 0.3	<40.03	<3.74	25.34	LERG
22	J085236.12+262013.6	0.477	—	—	41.34± 0.03	15.39 ± 1.27	25.24	HERG
23	J085915.19+080539.7	0.565	307 ± 90	9.3 ± 0.6	<40.69	<5.88	26.41	HERG
31	J092401.17+403457.1	0.160	399 ± 13	9.8 ± 0.2	<40.18	<0.60	24.94	LERG
33	J093014.90+234359.1	0.538	225 ± 51	8.7 ± 0.5	41.67± 0.05	10.36 ± 1.70	24.94	HERG
34	J093238.29+161157.2	0.191	249 ± 23	8.9 ± 0.2	41.82± 0.01	39.93 ± 0.59	26.00	HERG
37	J095640.76−000124.0	0.139	221 ± 25	8.7 ± 0.2	40.50± 0.05	2.91 ± 0.57	24.85	LERG
38	J100408.95+350623.6	0.611	312 ± 81	9.3 ± 0.5	42.19± 0.01	41.59 ± 1.60	25.74	HERG
39	J101028.09+530313.2	0.341	270 ± 47	9.1 ± 0.4	<40.46	<1.61	25.17	LERG
41	J101732.51+632953.7	0.184	245 ± 15	8.9 ± 0.2	40.85± 0.03	4.55 ± 0.48	24.59	LERG
44	J103900.86+354050.1	0.569	—	—	<41.03	<5.35	24.88	HERG
45	J103924.92+464811.6	0.531	414 ± 35	9.9 ± 0.3	41.22± 0.06	4.62 ± 0.92	25.65	LERG
49	J112848.71+171104.6	0.347	214 ± 28	8.6 ± 0.3	<40.26	<1.38	26.23	LERG
51	J113816.61+495025.3	0.510	335 ± 50	9.5 ± 0.4	41.53± 0.02	12.55 ± 0.95	26.29	HERG
52	J114522.18+152943.2	0.068	263 ± 7	9.0 ± 0.2	39.48± 0.11	0.63 ± 0.29	26.09	LERG
56	J122550.50+163343.4	0.656	—	—	42.16± 0.02	55.92 ± 3.05	25.34	HERG
57	J125721.88+122820.6	0.208	229 ± 37	8.8 ± 0.3	41.00± 0.02	6.80 ± 0.48	25.93	HERG
61	J130854.24+225822.1	0.677	188 ± 65	8.4 ± 0.6	< 41.00	< 4.9	25.93	LERG
67	J132939.94+181841.9	0.514	—	—	41.67± 0.02	28.37 ± 2.97	26.76	HERG
69	J133051.02+024843.2	0.623	201 ± 64	8.5 ± 0.6	<40.91	<3.59	25.72	LERG
70	J134002.96+503539.8	0.232	242 ± 17	8.9 ± 0.2	40.66± 0.06	3.79 ± 1.01	24.80	LERG
74	J140349.80+495305.4	0.491	—	—	41.95± 0.01	56.58 ± 1.62	26.34	HERG
84	J150904.13+212415.1	0.311	275 ± 27	9.1 ± 0.3	< 40.57	<2.52	25.64	LERG
93	J160809.56+294514.8	0.226	236 ± 21	8.8 ± 0.2	41.18± 0.02	10.92 ± 0.84	26.50	HERG
95	J162245.42+070714.7	0.597	234 ± 73	8.8 ± 0.6	41.88± 0.03	22.62 ± 1.79	26.50	HERG
96	J164857.36+260441.1	0.137	209 ± 22	8.6 ± 0.3	40.24± 0.09	3.25 ± 1.16	26.24	LERG
104	J223628.90+042751.7	0.303	306 ± 29	9.3 ± 0.3	41.17± 0.02	12.33 ± 0.92	26.23	HERG

positions was accepted). For each host galaxy, infrared colors were then calculated using their magnitudes given for the three mid-IR bands of the *WISE* survey [$W1(3.4\mu\text{m})$, $W2(4.6\mu\text{m})$ and $W3(12\mu\text{m})$ in Vega magnitudes]. Fig. 8 shows the color-color diagram for the 74 XRGs and 235 FR II radio galaxies, which were detected in all three *WISE* bands ($W1$, $W2$ and $W3$). It is noteworthy that the XRGs are typically found to be infra-redder than the FR IIs, with a large fraction $\sim 80\%$ (59/74) actually falling in the region populated by spiral galaxies, i.e., the *WISE* $W2 - W3$ color index being > 1.5 mag. In contrast, only $\sim 20\%$ of the FR II radio galaxies are found to inhabit that space. This indicates that compared to FR II radio galaxies, XRGs have a greater abundance of cool ISM, probably contributed by a recent merger. Note also that Stern et al. (2012) have suggested that $W1 - W2 \geq 0.8$ cut can be used to identify the most powerful AGNs with a high degree of reliability. Employing this clue, we find that 16 out of the 74 XRGs (i.e., $\sim 22\%$) plotted in Fig. 8 host a powerful AGN. This fraction would rise to 40% if

a less stringent color cut of $W1 - W2 \geq 0.6$ is adopted, following Wright et al. (2010).

The *WISE* color data have also been found useful for classifying radio galaxies into low- and high-excitation classes (LERGs and HERGs) (see, Gürkan et al. 2014). Sadler et al. (2014) have shown that nearly all the HERGs in their sample have the color index ($W2 - W3 \gtrsim 2$). Using the 2712 nearby radio-luminous galaxies, Yang et al. (2015) have shown that LERGs and HERGs have different mid-infrared properties, such that in the *WISE* color-color diagram the two excitation classes are separated by color index $W1 - W2 = 0.4$, albeit with a significant overlap between the two populations (see, also Pace & Salim 2016). We have applied the above two selection filters, namely $W1 - W2 < 0.4$ and $W2 - W3 < 2$ to estimate the fraction of LERGs and found that 20 out of 74 ($\sim 30\%$) of the *WISE* detected XRGs are consistent with the LERG classification. However, bearing in mind the fairly large uncertainty in this estimate (Pace & Salim 2016), the rather modest fraction of LERGs inferred here may not be inconsistent with the higher LERG fraction ($\sim 50\%$) inferred above

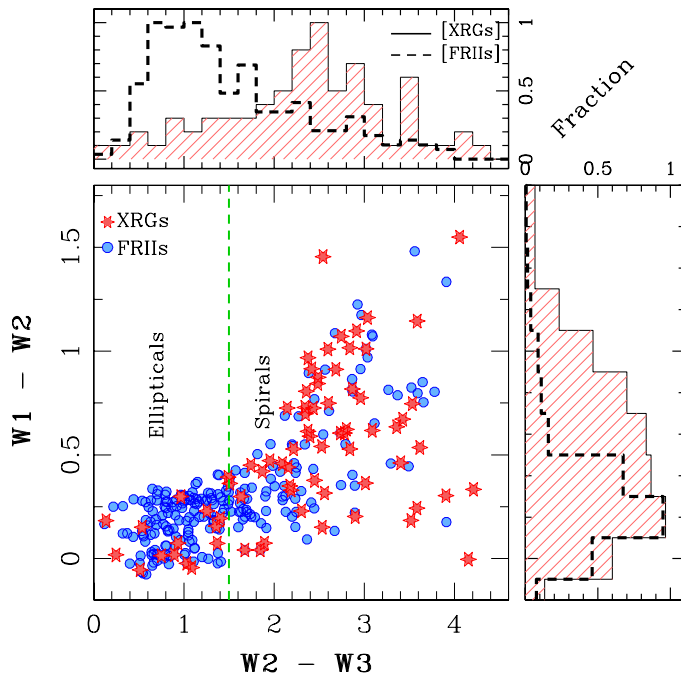


Figure 8. The *WISE* color-color diagram drawn for XRGs (stars) and FRII radio galaxies (circles). The green dashed line with $W2 - W3 = 1.5$ marks the division between elliptical and spiral galaxies (Wright et al. 2010). The top and right-hand panels display the distributions of $W2 - W3$ and $W1 - W2$ colors, respectively.

for XRGs, from optical spectroscopic classification (see Section 4.2), and also by Gillone et al. (2016), who found similar fractions of LERGs and HERGs among XRGs.

4.4. The environmental influence

The origin of the FRI and FRII dichotomy among radio galaxies has been debated for a long time. According to one viewpoint, its origin is intrinsic, related to the central SMBH and/or the physical conditions in the accretion flow, such that FRIs are preferentially LERGs and FRIIs are mostly HERGs (Marchesini et al. 2004; Hardcastle et al. 2006; Kauffmann et al. 2008). In the alternative proposition, their difference is attributed to the interactions of the jets with the gaseous environment of the host galaxy (Kawakatu et al. 2009; Lin et al. 2010; Capetti et al. 2017). In this scenario, FRI radio galaxies are deemed to be powered by weaker central engines and their (weaker) jets are influenced by the ambient circum-galactic medium to a greater degree, such that their (less powerful) jets propagating through a denser medium experience a greater resistance, which then leads to an FRI morphology (Gopal-Krishna & Wiita 1988, 2000, 2001; Kaiser & Best 2007). Several studies have con-

firmed a higher abundance of FRI radio galaxies in denser environment, as compared to FRII radio galaxies (Gendre et al. 2013; Rodman et al. 2019).

We have measured the clustering environment around the XRGs and also for the control sample of FRII radio galaxies, within a (projected) radius of 1 Mpc and a (photometric) redshift interval of $\pm 0.04(1+z)$ around the spectroscopic (or, alternatively, photometric) redshift, z , of a given radio galaxy. Within these spatial and redshift bounds, we counted the number of SDSS galaxies with absolute magnitudes brighter than $M_r = -19$ and determined the clustering richness (N_1^{-19}) of the environment by subtracting the number of background galaxies (brighter than $M_r = -19$ found within an annulus with inner and outer radii of 2.7 and 3.0 Mpc measured from the radio source position (Wen et al. 2012; Gendre et al. 2013). In order to minimize the incompleteness in the galaxy counts arising from the adopted magnitude limit, as dictated by the SDSS photometric data, as well as the steeply growing uncertainty in redshift estimation at higher redshifts, we only selected galaxies having photo- $z < 0.4$. This search, based on the SDSS archival data, covered all the 225 XRGs, including our 106 ‘strong’ cases and the 119 XRGs assembled by Cheung (2007), as well as our control sample of 388 FRII radio galaxies (see above). We found 107 XRGs and 343 FRII radio galaxies that satisfied the above selection filters of $z < 0.4$ and $M_r \leq -19$, and determined the clustering environment around them, following the aforesaid procedure.

The derived distributions of the cluster richness for the sample of XRGs and the control sample of FRII radio galaxies are compared in Fig. 9. It is evident that XRGs and FRIIs inhabit similar weak clustering environments, the median cluster richnesses being 8.94 and 11.87, respectively. Both values correspond to a ‘poor’ cluster environment. The shaded gray region in Fig. 9 marks the $N_1^{-19} > 30$, normally regarded as the rough boundary separating poor from rich clusters (Gendre et al. 2013). The present analysis shows that, very similarly, the vast majority of XRGs (91 out of 107, i.e., $\sim 85\%$) and of the FRII radio galaxies (291 out of 343, i.e., $\sim 84\%$) reside in poor environments. A similar median richness of 14.9 has been found by Gendre et al. (2013) for FRII radio sources. They also have confirmed that FRI sources reside in relatively dense environments, with median richness of 29.8, seemingly consistent with the premise that the (weaker) jets of FRI sources, propagating in denser media, are more prone to disruption (see above). Thus, the preponderance of XRGs in poor clustering environment appears in tune with the finding that they mostly belong to the FRII class (see

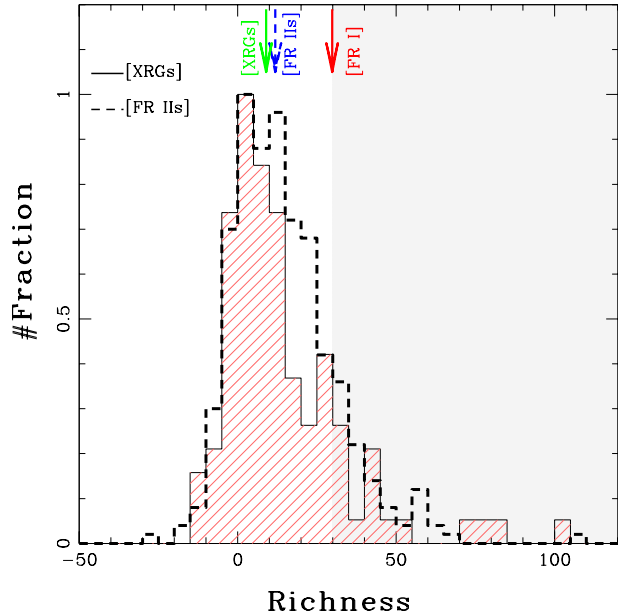


Figure 9. Distribution of the environmental richness factor for XRGs (hatched histogram) and FR II radio galaxies (dashed curve). The median richnesses for the XRGs and FR II are marked as solid and dashed arrows, respectively, together with the median estimated richness for FRI radio galaxies (Gendre et al. 2013). The gray shaded region corresponds to rich clustering environment, with richness > 30 , the boundary taken to separate poorer from richer clusters (Gendre et al. 2013).

section 5 of Saripalli & Subrahmanyan 2009), and also Kuźmicz et al. (2019).

5. DISCUSSION AND CONCLUSION

In this study we have investigated the nature of X-shaped radio galaxies (XRGs) by examining possible connections between their radio and optical morphologies, their optical spectral properties as well as the clustering environment around their host galaxies. The principal trigger for this study came from a catalog of XRGs, recently published by some of us (Yang et al. 2019) which contains 106 ‘strong’ XRG candidates. We have used it for examining the geometrical relationship between the axes of their radio structure and the apparent orientation of the parent elliptical galaxies. This was possible for 41 of the XRGs for which the position angle of the optical major axis of the parent elliptical galaxy could be determined with a fair degree of reliability, primarily using their SDSS i -band images.

The position angles of the primary radio axis (defined by the two active lobes) and the secondary radio axis (defined by the two wings) were measured by analyzing their FIRST 1.4 GHz maps, aided by the TGSS 150 MHz

maps (Section 3). This analysis has confirmed the previously reported strong tendency for the secondary radio axis to be closer to the optical minor axis (see the lower panel of Fig. 2). Quantitatively, the directional offset between the wings’ axis from the optical major axis is found to exceed 30° (median 56°) in $\sim 68\%$ of the XRGs. The KS -test rejects the null probability of being drawn from a uniform distribution at 0.05 significance level. Thus, our analysis strengthens the earlier findings based on smaller samples of XRGs (e.g., by Capetti et al. 2002 and Gillone et al. 2016), which is basically in accord with the scenario that the radio wings in XRGs probably arise from diversion of the back-flowing synchrotron plasma of the two primary lobes, by an asymmetric circum-galactic medium of the host galaxy (Section 1). This is also seen in the recent 3D relativistic magnetohydrodynamic simulations of the twin-jets propagating in a triaxial density distribution, by Rossi et al. (2017), see also, Hodges-Kluck & Reynolds (2011). We note, however, this does not preclude alternative scenarios proposed for the origin of the wings, e.g., the spin-flip mechanism (Section 1). This possibility is also favored by the finding that a non-negligible fraction (6 out of 41) of XRGs are counter-examples to this trend, wherein the secondary radio axis, defined by the wings, lies closer to the optical main axis of the parent elliptical galaxy (Section 3). Earlier, only one such counter-example had been reported by Gillone et al. (2016) (1 out of 22 XRGs in their sample). However, in that source even the sole visible radio wing has a very low surface brightness, rendering its position angle estimate quite uncertain. For the present, at least for the counter-examples, an alternative mechanisms (Section 1), like the spin-flip scenario (or some variant of it) could offer a greater promise.

In the jet-shell interaction scenario, a (*transverse*) radio wing develops as the jet’s head gets nearly stalled temporarily due to its interception by a (rotating) shell segment. The synchrotron plasma deposited at the jet’s head would then undergoes a (*transverse*) diversion due to dragging by the shell, until the jet’s blocking is over and its rapid advance resumes (GBGW12). A plausible example of this is witnessed in the radio galaxy 3C433 (Miller & Brandt 2009, see Fig. 1 of GBGW12). Since a similar interruption is likely to be experienced by the counter-jet (albeit not necessarily contemporaneous to the main jet), a Z-symmetric morphology of the radio wings can be expected to result. Note that in this jet-shell interaction scenario, the wing’s extent is mainly determined by the duration for which the jet remains quasi-stalled by the shell, as compared to the subsequent phase during which the jet propagates freely ahead. It is then easily conceivable that the wing becomes longer

than the primary lobe, as indeed found in roughly a fifth of XRGs (Fig. 4) to the detriment of the basic backflow diversion scenario.

Another important ramification of this scenario is that the launching point of the wing (due to transverse diversion of the jet’s synchrotron plasma) would coincide with the arresting of the jet’s head by the intercepting shell. Since this could well take place dozens of kiloparsec away from the host galaxy, the existence of large radio wings at such huge radial distances from the parent galaxy can be readily understood, unlike the model which attributes the wing formation to diversion of the backflowing plasma in the primary lobes, by a non-spherical interstellar medium of the parent galaxy (Section 1). The existence of several cases of wings originating so far away from the galaxies, has recently prompted the classification of the wings into two types (Saripalli & Roberts 2018). According to these authors, wings are launched from the active lobes at two ‘strategic’ locations, such that the preferred launching points are either fairly close to the parent galaxy (i.e., within its ISM), or, alternatively just somewhat behind jet’s head (i.e., hot spot). They have termed the two types as the inner (‘I-dev’) and outer (‘O-dev’) type wings. Whereas the I-dev type wings, quite likely involve interaction with the ISM of the host galaxy, which therefore defines their physical scale, the preferred location of the ‘O-dev’ type wings seems enigmatic. However, this may be easily understood in the jet-shell interaction model for the wing formation. In this scenario, the growth of the wing peaks during the phase when the growth of the primary lobe remains muted as the jet’s head remains nearly stalled by the intercepting shell sedgement (and, consequently, the backflow of the synchrotron plasma intensifies). We propose that the occurrence of the two processes in tandem could explain the propensity of the ‘O-dev’ type wings to be found to be footed only a short way behind the jet head (see above).

The ‘backflow diversion’ scenario may also hold a clue to the intriguing result that in several XRGs, radio spectral variations are too small to reveal any sign of radiative aging in the wings (see, Lal et al. 2019, and refs. therein). As the younger synchrotron plasma backflowing in the primary lobes, continues to be diverted into the existing cavities filled by the (low density) synchrotron plasma of the wings, this would keep the wings supplied with younger synchrotron plasma, thereby prolonging their radiative lifespans (see, also GBGW12; Hodges-Kluck & Reynolds 2012; Saripalli & Roberts 2018).

Comparing the mid-infrared properties of the 74 XRGs and a control sample of 235 FR II radio galaxies

with their counterparts in the *WISE* catalog, we have shown that a large fraction $\sim 80\%$ (59/74) of XRGs have redder hosts, with $W2 - W3 > 1.5$. In contrast, only $\sim 20\%$ of the FR II radio galaxies are found to inhabit that colour space (Fig. 8). This mid-IR colour difference is indicative of a higher abundance of dusty ISM in XRGs, possibly contributed by a recent galaxy merger. A similar effect has been noticed for double-double radio galaxies Kuźmicz et al. (2017). Thus, galaxy merger appears to be an especially important aspect of both these classes of radio galaxies and should feature in their theoretical modelling.

One arena where XRGs display striking similarity to normal FR II radio galaxies is the large-scale clustering environment around their host galaxies. In this work, we have compared the galaxy clustering densities around 107 XRGs and 343 FR II radio galaxies at $z < 0.4$, counting the $M_r \geq -19$ galaxies seen within 1 megaparsec and within a redshift interval of $\Delta z = 0.04(1+z)$. Our analysis shows that both XRGs and FR IIs inhabit relatively poor environments, with median cluster richness of 8.9 and 11.87, respectively (also see, Gendre et al. 2013). In comparison, FR I radio galaxies with less well collimated radio jets are known to inhabit significantly richer environment, with median richness of ~ 30 (see, Gendre et al. 2013). This clearly reflects the role played by the clustering environment in the XRG phenomena.

In summary, the present study shows that the remarkable diversity in the observed properties of XRGs is hard to encompass within a single physical mechanism (i.e, backflow diversion via over-pressured cocoons, or a rapid reorientation of the AGN axis, or the jet-shell interaction scenario). It appears that several mechanism are at work, and their relative importance may differ among the sources. In particular, a clearer insight would require deeper optical and possibly X-ray imaging of the parent galaxies of XRGs, combined with their radio spectral mapping.

ACKNOWLEDGMENTS

We thank the anonymous referee for constructive comments and suggestions. This work was supported by the China Postdoctoral Science Foundation Grants (2018M630024, 2019T120011), the National Key R&D Program of China (2016YFA0400702, 2016YFA0400703) and the National Science Foundation of China (11473002, 11721303, 11533001). SS acknowledges support from the Science and Engineering Research Board, India, through the Ramanujan Fellowship.

Funding for the Sloan Digital Sky Survey IV has been provided by the Alfred P. Sloan Foundation, the U.S.

Department of Energy Office of Science, and the Participating Institutions. SDSS-IV acknowledges support and resources from the Center for High-Performance Computing at the University of Utah. The SDSS web site is www.sdss.org.

SDSS-IV is managed by the Astrophysical Research Consortium for the Participating Institutions of the SDSS Collaboration including the Brazilian Participation Group, the Carnegie Institution for Science, Carnegie Mellon University, the Chilean Participation Group, the French Participation Group, Harvard-Smithsonian Center for Astrophysics, Instituto de Astrofísica de Canarias, The Johns Hopkins University, Kavli Institute for the Physics and Mathematics of the Universe (IPMU) / University of Tokyo, Lawrence Berkeley National Laboratory, Leibniz Institut für As-

trophysik Potsdam (AIP), Max-Planck-Institut für Astronomie (MPIA Heidelberg), Max-Planck-Institut für Astrophysik (MPA Garching), Max-Planck-Institut für Extraterrestrische Physik (MPE), National Astronomical Observatories of China, New Mexico State University, New York University, University of Notre Dame, Observatório Nacional / MCTI, The Ohio State University, Pennsylvania State University, Shanghai Astronomical Observatory, United Kingdom Participation Group, Universidad Nacional Autónoma de México, University of Arizona, University of Colorado Boulder, University of Oxford, University of Portsmouth, University of Utah, University of Virginia, University of Washington, University of Wisconsin, Vanderbilt University, and Yale University.

REFERENCES

- Begelman, M. C., Blandford, R. D., & Rees, M. J. 1984, *Reviews of Modern Physics*, 56, 255
- Best, P. N., & Heckman, T. M. 2012, *MNRAS*, 421, 1569
- Capetti, A., Massaro, F., & Baldi, R. D. 2017, *A&A*, 601, A81
- Capetti, A., Zamfir, S., Rossi, P., et al. 2002, *A&A*, 394, 39
- Cappellari, M. 2017, *MNRAS*, 466, 798
- Cappellari, M., & Emsellem, E. 2004, *PASP*, 116, 138
- Carter, D., Allen, D. A., & Malin, D. F. 1982, *Nature*, 295, 126
- Cheung, C. C. 2007, *AJ*, 133, 2097
- Dennett-Thorpe, J., Scheuer, P. A. G., Laing, R. A., et al. 2002, *MNRAS*, 330, 609
- Dey, A., Schlegel, D. J., Lang, D., et al. 2018, *arXiv e-prints*. <https://arxiv.org/abs/1804.08657>
- Ferrarese, L., Pogge, R. W., Peterson, B. M., et al. 2001, *ApJ*, 555, L79
- Gebhardt, K., Bender, R., Bower, G., et al. 2000, *ApJ*, 539, L13
- Gendre, M. A., Best, P. N., Wall, J. V., & Ker, L. M. 2013, *MNRAS*, 430, 3086
- Gillone, M., Capetti, A., & Rossi, P. 2016, *A&A*, 587, A25
- Gopal-Krishna, Biermann, P. L., de Souza, V., & Wiita, P. J. 2010, *ApJ*, 720, L155
- Gopal-Krishna, Biermann, P. L., Gergely, L. Á., & Wiita, P. J. 2012, *Research in Astronomy and Astrophysics*, 12, 127
- Gopal-Krishna, Biermann, P. L., & Wiita, P. J. 2003, *ApJ*, 594, L103
- Gopal-Krishna, & Chitre, S. M. 1983, *Nature*, 303, 217
- Gopal-Krishna, & Saripalli, L. 1984, *A&A*, 141, 61
- Gopal-Krishna, & Wiita, P. J. 1988, *Nature*, 333, 49
- . 2000, *A&A*, 363, 507. <https://arxiv.org/abs/astro-ph/0009441>
- . 2001, *A&A*, 373, 100
- Greene, J. E., & Ho, L. C. 2004, *ApJ*, 610, 722
- Gürkan, G., Hardcastle, M. J., & Jarvis, M. J. 2014, *MNRAS*, 438, 1149
- Hardcastle, M. J., Evans, D. A., & Croston, J. H. 2006, *MNRAS*, 370, 1893
- Hodges-Kluck, E., & Bregman, J. N. 2014, *ApJ*, 789, 131
- Hodges-Kluck, E. J., & Reynolds, C. S. 2011, *ApJ*, 733, 58
- . 2012, *ApJ*, 746, 167
- Hodges-Kluck, E. J., Reynolds, C. S., Cheung, C. C., & Miller, M. C. 2010a, *ApJ*, 710, 1205
- Hodges-Kluck, E. J., Reynolds, C. S., Miller, M. C., & Cheung, C. C. 2010b, *ApJ*, 717, L37
- Jedrzejewski, R. I. 1987, *MNRAS*, 226, 747
- Kaiser, C. R., & Best, P. N. 2007, *MNRAS*, 381, 1548
- Kauffmann, G., Heckman, T. M., & Best, P. N. 2008, *MNRAS*, 384, 953
- Kawakatu, N., Kino, M., & Nagai, H. 2009, *ApJ*, 697, L173
- Kewley, L. J., Groves, B., Kauffmann, G., & Heckman, T. 2006, *MNRAS*, 372, 961
- Kharb, P., Lal, D. V., & Merritt, D. 2017, *Nature Astronomy*, 1, 727
- Kormendy, J., & Ho, L. C. 2013, *Annual Review of Astronomy and Astrophysics*, 51, 511
- Kozieł-Wierzbowska, D., & Stasińska, G. 2011, *MNRAS*, 415, 1013
- Kraft, R. P., Hardcastle, M. J., Worrall, D. M., & Murray, S. S. 2005, *ApJ*, 622, 149
- Kuzmicz, A., Czerny, B., & Wildy, C. 2019, *A&A*, 624, A91

- Kuźmicz, A., Jamrozy, M., Koziel-Wierzbowska, D., & Weżgowiec, M. 2017, *MNRAS*, 471, 3806
- Lal, D. V., & Rao, A. P. 2005, *MNRAS*, 356, 232
- . 2007, *MNRAS*, 374, 1085
- Lal, D. V., Sebastian, B., Cheung, C. C., & Pramesh Rao, A. 2019, arXiv e-prints, arXiv:1903.11632.
<https://arxiv.org/abs/1903.11632>
- Landt, H., Cheung, C. C., & Healey, S. E. 2010, *MNRAS*, 408, 1103
- Leahy, J. P., & Parma, P. 1992, in *Extragalactic Radio Sources. From Beams to Jets*, ed. J. Roland, H. Sol, & G. Pelletier, 307–308
- Leahy, J. P., & Williams, A. G. 1984, *MNRAS*, 210, 929
- Lin, Y.-T., Shen, Y., Strauss, M. A., Richards, G. T., & Lunnan, R. 2010, *ApJ*, 723, 1119
- Mancillas, B., Combes, F., & Duc, P.-A. 2019, arXiv e-prints, arXiv:1905.11356.
<https://arxiv.org/abs/1905.11356>
- Marchesini, D., Celotti, A., & Ferrarese, L. 2004, *MNRAS*, 351, 733
- Merritt, D., & Ekers, R. D. 2002, *Science*, 297, 1310
- Mezcua, M., Chavushyan, V. H., Lobanov, A. P., & León-Tavares, J. 2012, *A&A*, 544, A36
- Mezcua, M., Lobanov, A. P., Chavushyan, V. H., & León-Tavares, J. 2011, *A&A*, 527, A38
- Miller, B. P., & Brandt, W. N. 2009, *ApJ*, 695, 755
- Oosterloo, T. A., & Morganti, R. 2005, *A&A*, 429, 469
- Pace, C., & Salim, S. 2016, *ApJ*, 818, 65
- Ramos Almeida, C., Tadhunter, C. N., Inskip, K. J., et al. 2011, *MNRAS*, 410, 1550
- Rawlings, S., Saunders, R., Eales, S. A., & Mackay, C. D. 1989, *MNRAS*, 240, 701
- Roberts, D. H., Saripalli, L., Wang, K. X., et al. 2018, *ApJ*, 852, 47
- Rodman, P. E., Turner, R. J., Shabala, S. S., et al. 2019, *MNRAS*, 482, 5625
- Rodriguez, C., Taylor, G. B., Zavala, R. T., et al. 2006, *ApJ*, 646, 49
- Rossi, P., Bodo, G., Capetti, A., & Massaglia, S. 2017, *A&A*, 606, A57
- Rottmann, H. 2001, PhD thesis, -
- Rubinur, K., Das, M., & Kharb, P. 2019, *MNRAS*, 484, 4933
- Sadler, E. M., Ekers, R. D., Mahony, E. K., Mauch, T., & Murphy, T. 2014, *MNRAS*, 438, 796
- Saripalli, L., & Roberts, D. H. 2018, *ApJ*, 852, 48
- Saripalli, L., & Subrahmanyan, R. 2009, *ApJ*, 695, 156
- Schiminovich, D., van Gorkom, J. H., van der Hulst, J. M., & Kasow, S. 1994, *ApJ*, 423, L101
- Schlegel, D. J., Finkbeiner, D. P., & Davis, M. 1998, *ApJ*, 500, 525
- Schoenmakers, A. P., de Bruyn, A. G., Röttgering, H. J. A., van der Laan, H., & Kaiser, C. R. 2000, *MNRAS*, 315, 371
- Sikkema, G., Carter, D., Peletier, R. F., et al. 2007, *A&A*, 467, 1011
- Stasińska, G., Cid Fernandes, R., Mateus, A., Sodré, L., & Asari, N. V. 2006, *MNRAS*, 371, 972
- Stern, D., Assef, R. J., Benford, D. J., et al. 2012, *ApJ*, 753, 30
- Struve, C., & Conway, J. E. 2010, *Astronomy and Astrophysics*, 513, A10
- Tadhunter, C. 2016, *A&A Rev.*, 24, 10
- Tremaine, S., Gebhardt, K., Bender, R., et al. 2002, *ApJ*, 574, 740
- Vazdekis, A., Sánchez-Blázquez, P., Falcón-Barroso, J., et al. 2010, *MNRAS*, 404, 1639
- Wen, Z. L., Han, J. L., & Liu, F. S. 2012, *ApJS*, 199, 34
- Wilson, A. S., & Colbert, E. J. M. 1995, *ApJ*, 438, 62
- Worrall, D. M., Birkinshaw, M., & Cameron, R. A. 1995, *ApJ*, 449, 93
- Wright, E. L., Eisenhardt, P. R. M., Mainzer, A. K., et al. 2010, *AJ*, 140, 1868
- Yang, X., Joshi, R., Gopal-Krishna, et al. 2019, arXiv e-prints. <https://arxiv.org/abs/1905.06356>
- Yang, X.-h., Chen, P.-s., & Huang, Y. 2015, *MNRAS*, 449, 3191
- Zhang, X.-G., Dultzin-Hacyan, D., & Wang, T.-G. 2007, *MNRAS*, 377, 1215
- Zier, C., & Biermann, P. L. 2001, *A&A*, 377, 23
- . 2002, *A&A*, 396, 91

6. APPENDIX

Table 3. Radio and optical parameters of X-shaped radio galaxies.

Id	Name	Active-lobe		Passive-lobe		Optical	Ellipticity	flag ^b
		PA ^a (°)	length (")	PA (°)	length (")	PA (°)		
1	J000450.27+124839.52	286/ 101	172.4/ 148.9	53/ 245	126.1/ 133.6	53 ± 12	0.153 ± 0.031	1
2	J002828.94−002624.60	47/ 226	80.0/ 104.2	15/ 214	83.2/ 104.4	123 ± 9	0.199 ± 0.038	1
3	J003023.86+112112.50	61/ 241	39.2/ 38.9	19/ 180	20.5/ 23.5	25 ± 7	0.271 ± 0.016	1
4	J012101.23+005100.38	360/ 178	23.4/ 21.1	90/ 266	18.2/ 12.0	30 ± 7	0.397 ± 0.071	1
5	J021635.79+024400.90	12/ 190	62.1/ 67.9	80/ 272	23.6/ 18.9	118 ± 9	0.188 ± 0.035	1
6	J031937.58−020248.70	291/ 113	17.5/ 14.9	344/ 163	27.2/ 24.2	118 ± 5	0.301 ± 0.032	1 [†]
7	J071031.14+354649.80	8/ 185	22.1/ 25.3	316/ 139	18.3/ 20.2	—	—	0 [†]
8	J071510.12+491053.28	291/ 123	17.7/ 18.6	26/ 213	13.4/ 18.0	138 ± 3	0.084 ± 0.037	0
9	J072014.66+403748.68	291/ 110	16.9/ 18.9	30/ 202	13.1/ 20.2	87 ± 7	0.079 ± 0.074	0
10	J072737.48+395655.84	255/ 45	23.7/ 11.1	306/ 220	19.9/ 14.6	—	—	2
11	J075249.10+325254.20	12/ 180	20.9/ 24.6	288/ 71	23.5/ 18.4	50 ± 3	0.047 ± 0.048	0
12	J075445.52+242425.30	35/ 204	17.2/ 12.0	305/ 108	14.4/ 23.7	93 ± 2	0.218 ± 0.025	1
13	J075930.94+124722.86	8/ 185	20.5/ 21.7	298/ 123	10.1/ 18.0	—	—	3
14	J080006.84+495755.06	296/ 123	16.8/ 19.1	169/ 188	20.3/ 25.8	—	—	4
15	J081337.78+300710.60	283/ 90	20.8/ 21.8	21/ 220	16.7/ 15.1	—	—	3
16	J081404.55+060238.38	29/ 198	23.6/ 24.9	312/ 130	21.6/ 29.1	24 ± 5	0.143 ± 0.050	1
17	J081601.88+380415.48	71/ 263	22.8/ 21.1	9/ 180	18.4/ 20.5	14 ± 2	0.372 ± 0.011	1
18	J081841.57+150833.50	314/ 116	14.4/ 17.1	46/ 225	14.6/ 17.1	146 ± 2	0.194 ± 0.042	1
19	J082226.42+051951.16	60/ 230	31.9/ 27.0	356/ 135	22.0/ 21.9	—	—	0
20	J082400.50+031749.30	57/ 252	20.7/ 23.9	307/ 108	34.5/ 23.5	12 ± 4	0.420 ± 0.010	1
21	J084509.65+574035.54	9/ 180	13.3/ 13.1	277/ 90	15.0/ 15.0	165 ± 3	0.296 ± 0.032	1
22	J085236.12+262013.41	315/ 135	23.7/ 22.7	515/ 249	13.1/ 16.3	—	—	0
23	J085915.19+080539.72	84/ 262	14.9/ 13.0	8/ 110	14.8/ 18.1	—	—	0
24	J085942.66+585116.64	22/ 213	20.3/ 18.4	290/ 98	22.1/ 12.9	53 ± 9	0.223 ± 0.044	2
25	J085954.12−025241.93	347/ 161	17.6/ 22.6	287/ 110	26.4/ 19.1	160 ± 3	0.088 ± 0.028	0 [†]
26	J090331.03+560039.99	80/ 251	11.4/ 19.2	350/ 178	14.6/ 8.2	—	—	0
27	J090638.35+064524.62	290/ 180	18.4/ 15.8	90/ 231	14.7/ 12.9	—	—	0
28	J090827.86+215823.81	34/ 185	21.0/ 20.8	293/ 135	15.0/ 22.4	—	—	0
29	J091451.07+082440.17	304/ 128	13.5/ 12.9	60/ 238	12.9/ 19.2	—	—	0
30	J092346.43+361407.33	290/ 84	19.3/ 18.6	338/ —	19.0/ —	—	—	0
31	J092401.16+403457.29	45/ 232	23.1/ 21.7	3/ 185	36.8/ 24.4	27 ± 3	0.319 ± 0.025	1
32	J092802.68−060752.63	275/ 93	30.4/ 30.1	8/ 150	12.9/ 34.6	124 ± 2	0.178 ± 0.019	1 [†]
33	J093014.90+234359.20	43/ 223	33.0/ 43.8	339/ 185	17.1/ 17.0	114 ± 4	0.326 ± 0.043	1
34	J093238.30+161157.33	308/ 128	136.3/ 125.6	286/ 101	79.3/ 70.7	7 ± 3	0.054 ± 0.064	2
35	J094240.45+044423.10	290/ 112	18.5/ 15.6	28/ 231	9.8/ 13.4	—	—	0
36	J094953.64+445655.77	328/ 147	54.2/ 51.8	14/ 196	32.9/ 29.0	113 ± 9	0.165 ± 0.017	1
37	J095640.77−000123.99	323/ 140	63.3/ 65.4	1/ 200	48.6/ 63.4	54 ± 38	0.017 ± 0.023	0
38	J100408.95+350623.69	52/ 249	31.7/ 17.7	6/ 157	20.2/ 14.8	—	—	0
39	J101028.07+530313.06	—	—	—	—	3 ± 160	0.094 ± 0.049	0
40	J101134.80−060753.14	360/ 206	13.9/ 13.4	325/ 140	17.3/ 14.7	—	—	0 [†]
41	J101732.51+632953.82	290/ 119	22.3/ 24.1	62/ 228	23.5/ 25.4	—	—	2
42	J103118.85+044307.70	56/ 226	28.0/ 26.8	2905/ 127	18.8/ 19.1	—	—	0
43	J103358.55+353007.24	11/ 170	15.6/ 16.9	80/ 260	11.7/ 15.2	26 ± 1	0.148 ± 0.143	0
44	J103900.86+354050.12	73/ 255	31.0/ 34.9	288/ 116	20.5/ 13.0	—	—	0

Continued on next page

Table 3 – continued from previous page

45	J103924.92+464811.53	315/ 126	24.4/ 25.9	60/ 238	36.4/ 23.4	8 ± 3	0.271 ± 0.067	1
46	J104632.43–011338.15	27/ 219	32.6/ 29.5	90/ 264	16.6/ 18.7	147 ± 3	0.180 ± 0.007	1
47	J105426.39+470327.47	336/ 158	36.7/ 38.9	286/ 118	27.1/ 27.0	–	–	0
48	J110853.80+263650.20	45/ 248	18.6/ 19.1	297/ 110	10.3/ 18.9	–	–	0
49	J112848.72+171104.57	43/ 217	32.4/ 44.4	279/ 110	5.5/ 22.0	111 ± 3	0.167 ± 0.027	1
50	J113649.98+015121.34	69/ 252	17.3/ 24.3	5/ 188	21.6/ 13.2	78 ± 10	0.097 ± 0.083	0
51	J113816.62+495025.03	336/ 140	11.1/ 14.1	70/ 225	20.7/ 13.1	12 ± 3	0.037 ± 0.050	0
52	J114522.19+152943.26	66/ 239	18.9/ 22.8	288/ 159	24.3/ 17.1	48 ± 3	0.179 ± 0.024	1
53	J115225.55+201602.19	73/ 249	26.3/ 17.2	48/ 180	25.4/ 13.1	98 ± 15	0.062 ± 0.074	0
54	J115500.34+441702.22	725/ 252	28.9/ 36.9	324/ 166	25.8/ 23.7	73 ± 3	0.265 ± 0.006	1
55	J120251.32–033625.80	293/ 114	19.3/ 21.1	358/ 201	21.2/ 17.0	43 ± 5	0.140 ± 0.028	1
56	J122550.51+163343.50	284/ 1065	39.0/ 29.2	328/ 164	18.5/ 27.2	–	±	0
57	J125721.87+122820.58	333/ 167	45.0/ 44.1	42/ 226	14.4/ 84.7	162 ± 9	0.202 ± 0.033	1
58	J125900.79+203248.63	355/ 180	20.9/ 20.7	45/ 244	11.7/ 13.2	–	–	0
59	J130048.34+350527.35	287/ 119	26.8/ 24.2	310/ 180	29.6/ 25.7	–	–	3
60	J130258.46+511943.69	293/ 120	42.1/ 49.9	47/ 201	50.6/ 25.4	–	–	0
61	J130854.25+225822.30	72/ 242	23.8/ 23.7	306/ 130	17.2/ 14.9	–	–	0
62	J131226.65+183414.98	55/ 225	17.0/ 18.2	315/ 157	6.2/ 14.6	143 ± 3	0.557 ± 0.016	1
63	J131331.40+075802.51	341/ 1545	27.6/ 29.9	303/ 114	19.9/ 18.6	51 ± 5	0.308 ± 0.040	1
64	J132324.26+411515.01	288/ 111	21.0/ 17.6	340/ 225	21.9/ 22.5	94 ± 3	0.299 ± 0.021	1
65	J132404.20+433407.14	17/ 198	67.4/ 101.4	349/ 186	68.5/ 88.2	130 ± 6	0.155 ± 0.018	1
66	J132713.87+285318.19	285/ 115	55.8/ 49.9	45/ 225	47.1/ 4.0	90 ± 16	0.113 ± 0.032	1
67	J132939.95+181842.01	52/ 236	23.1/ 30.0	355/ 160	22.5/ 19.8	–	–	4
68	J133051.04+024843.10	338/ 158	36.1/ 44.1	16/ 240	27.5/ 21.7	133 ± 2	0.219 ± 0.022	1
69	J133636.06+431329.02	270/ 96	28.1/ 26.3	341/ 140	18.5/ 29.2	–	–	3
70	J134002.96+503539.72	34/ 211	34.4/ 33.2	276/ 87	18.2/ 38.2	100 ± 2	0.158 ± 0.008	1
71	J134051.19+374911.74	330/ 1527	36.7/ 45.6	357/ 180	27.0/ 30.4	43 ± 2	0.306 ± 0.009	1
72	J134353.97+193334.10	69/ 213	25.6/ 19.5	298/ 119	9.1/ 24.2	–	–	0†
73	J135518.04+094022.90	279/ 105	37.8/ 35.6	62/ 253	23.5/ 26.1	–	–	0
74	J140349.79+495305.45	28/ 214	40.7/ 20.7	290/ 64	18.7/ 9.5	–	–	0
75	J140742.26+272207.66	360/ 203	16.5/ 15.5	292/ 128	16.8/ 21.6	–	–	0†
76	J141702.13+201903.30	63/ 230	26.7/ 20.7	309/ 120	24.4/ 9.4	55 ± 2	0.080 ± 0.110	0
77	J142646.41+271223.63	298/ 118	28.4/ 27.2	62/ 175	23.5/ 21.7	–	–	0
78	J143756.45+351937.10	2/ 180	19.9/ 14.9	305/ 54	16.4/ 17.0	–	–	0
79	J144547.33–013045.77	96/ 266	17.5/ 26.0	315/ 180	17.3/ 13.3	–	–	0
80	J150016.24–045036.65	86/ 255	29.3/ 34.4	38/ 218	22.2/ 21.6	–	–	0†
81	J150636.54+074016.94	42/ 215	22.4/ 16.6	300/ 135	11.5/ 4.5	–	–	0
82	J150816.29+613756.32	83/ 262	14.4/ 13.8	346/ 136	14.8/ 10.9	–	–	0
83	J150855.22–073036.46	14/ 188	33.4/ 33.3	52/ 225	21.9/ 18.5	–	–	3†
84	J150904.13+212415.10	270/ 90	26.0/ 17.4	22/ 198	29.2/ 20.2	140 ± 2	0.227 ± 0.014	1
85	J151149.30+045536.17	315/ 135	18.6/ 17.3	96/ 251	21.9/ 18.9	–	–	0
86	J151704.61+212242.14	315/ 135	24.1/ 19.0	1/ 225	16.9/ 17.2	50 ± 7	0.241 ± 0.010	1
87	J152245.38–050404.36	322/ 142	32.9/ 31.6	287/ 105	25.6/ 35.2	–	–	4
88	J154202.85+121427.66	303/ 113	18.7/ 14.6	29/ 246	15.1/ 11.8	–	–	3
89	J154413.39+304401.16	31/ 210	33.7/ 35.1	356/ 162	27.4/ 24.0	–	–	0
90	J154719.43+213012.00	85/ 2266	11.3/ 13.8	336/ 175	11.8/ 14.5	–	–	3
91	J154842.66+014919.48	34/ 180	42.2/ 25.2	70/ 222	36.4/ 31.0	–	–	0
92	J155416.04+381132.57	64/ 238	16.9/ 25.9	360/ 203	13.3/ 14.9	103 ± 3	0.465 ± 0.017	1

Continued on next page

Table 3 – continued from previous page

93	J160809.55+294514.92	306/ 126	13.4/ 15.3	41/ 180	20.0/ 15.1	168 ± 2	0.225 ± 0.011	1
94	J160833.28+012231.04	36/ 2025	16.9/ 18.8	300/ 143	10.9/ 15.1	–	–	0
95	J162245.42+070714.69	287/ 107	25.6/ 25.9	72/ 250	24.1/ 20.2	114 ± 3	0.143 ± 0.008	1
96	J164857.36+260441.26	302/ 135	19.1/ 23.2	65/ 198	12.6/ 20.1	117 ± 6	0.217 ± 0.037	1
97	J171547.52+493840.22	308/ 131	22.7/ 20.8	5/ 206	14.8/ 13.1	95 ± 4	0.025 ± 0.051	2 [†]
98	J202855.27+003512.67	283/ 106	41.9/ 29.8	29/ 212	52.3/ 34.2	58 ± 6	0.228 ± 0.023	1
99	J203459.54+005221.41	59/ 251	22.4/ 22.4	355/ 180	22.3/ 13.1	88 ± 5	0.136 ± 0.030	1
100	J205823.53+031124.47	4/ 187	32.0/ 31.6	56/ 232	20.1/ 22.0	–	–	0
101	J210053.62–033516.66	17/ 200	26.5/ 19.4	328/ 80	18.6/ 25.5	97 ± 3	0.056 ± 0.038	0 [†]
102	J214731.06–035942.40	311/ 98	17.5/ 14.1	355/ 204	18.2/ 12.1	68 ± 5	0.114 ± 0.082	0
103	J222802.33–065354.84	272/ 97	24.6/ 21.1	69/ 249	25.7/ 25.8	–	–	0
104	J223628.89+042751.89	358/ 169	51.6/ 55.2	73/ 245	25.8/ 21.9	145 ± 8	0.245 ± 0.034	1
105	J232020.30–075319.36	33/ 210	42.2/ 42.3	354/ 166	20.2/ 23.5	73 ± 3	0.430 ± 0.004	1
106	J233259.28+024715.37	342/ 159	21.3/ 17.6	64/ 234	13.2/ 16.6	70 ± 2	0.065 ± 0.047	0

^aOptical and radio position angles are measured from north to east.

^bFlag disription, 1= secure detection ; 0 = faint source; 2= merging or two nearby objects; 3= host galaxy not detected; 4= not covered in SDSS or DeCaLS; † optical position angle is measured from DECaLS images.